ADVANCED FUNCTIONAL MATERIALS
www.afm-journal.de

Tailoring Plasmonic Bimetallic Nanocatalysts Toward Sunlight-Driven H_2 Production

*Matias Herran, Ana Sousa-Castillo, Chenghao Fan, Seunghoon Lee, Wei Xie, Markus Döblinger, Baptiste Auguié, and Emiliano Cortés**

Hybrid nanoparticles combining plasmonic and catalytic components have recently gained interest for their potential use in sunlight-to-chemical energy conversion. However, a deep understanding of the structure–performance that maximizes the use of the incoming energy remains elusive. Here, a suite of Au and Pd based nanostructures in core–shell and core-satellites configurations are designed and their photocatalytic activity for Hydrogen (H_2) generation under sunlight illumination is tested. Formic acid is employed as H_2 source. Core-satellite systems show a higher enhancement of the reaction upon illumination, compared to core–shell ones. Electromagnetic simulations reveal that a key difference between both configurations is the excitation of highly localized and asymmetric electric fields in the gap between both materials. In this scheme, the core Au particle acts as an antenna, efficiently capturing visible light via the excitation of localized plasmon resonances, while the surrounding Pd satellites transduce the locally-enhanced electric field into catalytic activity. These findings advance the understanding of plasmon-driven photocatalysis, and provide an important benchmark to guide the design of the next generation of plasmonic bimetallic nanostructures.

1. Introduction

The past few decades have witnessed a global search for clean and renewable energy sources, such as hydrogen (H_2).[1] Hydrogen benefits from a relatively high energy density and has already found successful applications in fuel cells and combustion processes, through its green exothermic reaction with oxygen (O_2).[2–4] The large, and growing global demand for H_2 is currently met by electrolysis of H_2O and methane reforming.[5] Both reactions require energy input, which, in turn, drives the search for sustainable energy sources.[6–8] Solar energy has recently shown strong potential to enable this reaction at scale and sustainably.[9] The capture of solar energy and subsequent conversion into chemical energy can be facilitated by suitably-engineered nanostructures. The characteristic light-harvesting properties of plasmonic nanoantennas make them ideal candidates for such applications.[10] Nanoparticles formed with plasmonic materials such as Au, Ag, Al, or Cu interact resonantly with light in the visible and near-IR region, through the excitation of localized plasmon resonances (LSPR). These resonances coincide with the spectral range where the sun presents the maximum in its light emission profile.[11–14] The resonant excitation of the free electron gas of these metallic nanoparticles by incident light, leads to locally-enhanced electric fields, generation of hot carriers and local heat. Each of these effects has been proposed to accelerate chemical reaction rates at the nanoparticle surface.[15–21] Although these plasmonic materials display enhanced

M. Herran, A. Sousa-Castillo, C. Fan, S. Lee, E. Cortés
Nanoinstitute Munich
Faculty of Physics
Ludwig-Maximilians-Universität München
80539 Munich, Germany
E-mail: emiliano.cortes@lmu.de

A. Sousa-Castillo
CINBIO
Universidade de Vigo
Vigo 36310, Spain

The ORCID identification number(s) for the author(s) of this article can be found under https://doi.org/10.1002/adfm.202203418.

DOI: 10.1002/adfm.202203418

C. Fan, W. Xie
Key Lab of Advanced Energy Materials Chemistry (Ministry of Education)
Renewable Energy Conversion and Storage Center College of Chemistry
Nankai University, Weijin Rd. 94, Tianjin 300071, China

S. Lee
Department of Chemistry
Dong-A University
Busan 49315, South Korea

S. Lee
Department of Chemical Engineering (BK21 FOUR Graduate Program)
Dong-A University
Busan 49315, South Korea

M. Döblinger
Department of Chemistry
Ludwig-Maximilians-Universität München
Butenandtstr. 5–13 (E), 81377 Munich, Germany

B. Auguié
The MacDiarmid Institute for Advanced Materials and Nanotechnology
School of Chemical and Physical Sciences
Victoria University of Wellington
Wellington 6140, New Zealand

catalytic properties upon illumination, they are intrinsically poor catalysts compared to other metals. Essentially, this is due to the fact that their Fermi level lies in an s-band. Conversely, metals where the Fermi level falls in a d-band (Pt, Rh, or Pd) have historically shown a superior affinity to bind molecules, owing to the better hybridization between the d-band of these metals and the lowest unoccupied molecular orbitals (LUMO) of the adsorbates.[6,22–24] This motivates the design of hybrid materials aiming to combine the light harvesting properties of plasmonic nanoparticles, with the catalytic properties of the d-band metals.[25–29]

Understanding the physical and chemical factors that dictate the efficient transfer of energy, from plasmon-enhanced light absorption to the active catalyst sites is a central open question for the future development and success of the field.[30] It is not sufficient to simply combine good energy harvesters—a plasmonic particle—, and good charge injectors—a catalytic metal—, one must also consider carefully how they interact.[26] A successful combination of both materials should be engineered to exploit the plasmon excitation for both its light-harvesting properties, but also for the conversion and transfer of energy to the catalyst surface where reactions takes place.[31] Injection of plasmonic hot-electrons into a catalytic material has been reported for core–shell structures,[16,32] near-field induced enhanced absorption on catalytic metals for core-satellites,[33–36] and even temperature-induced reactions (via lattice phonons) for self-assembled structures.[37] In all these reported structures, the spatial arrangement of the plasmonic—catalytic pair is crucial for the energy flow optimization: some of the pathways need metals to be either in direct contact, to be separated by small gaps or to be well separated; others even require metals to be mixed at the atomic scale (alloys). There is currently little clarity as to which of these designs leads to the most efficient redistribution pathway of the energy harvested by the plasmonic particle and transduced by the catalytic material. The design rules leading to the most efficient hybrid plasmonic catalysts are still largely unknown and form arguably one of the greatest current challenges nowadays in the field, despite considerable progress on both experimental and theoretical fronts.[33,38,39] Hence, the aim of this study is to tackle the unresolved question of which of the aforementioned structures energizes the catalytic metals the most.

In this work, we carefully designed experiments to compare four different combinations of Au and Pd components for H_2 generation under simulated sunlight illumination conditions. Formic acid (FA) decomposition was chosen as a model reaction. While Au was used as the plasmonic metal for its remarkable chemical stability, Pd was chosen as catalytic material since it presents a large activity for the target reaction. Au@Pd and Au@AuPd core–shell and their corresponding core-satellites configuration were fabricated using previously synthesized Au nanospheres (Au NS) as building blocks. The surface chemistry of the catalysts was tuned in order to minimize differences among the systems and to properly assess the light harvesting efficiency. Thus, the remarkable control on the catalysts architecture, reaction conditions, and the surface chemistry of the catalysts, as well as the convection conditions, enabled us to focus on which structure maximizes the sunlight absorption and catalytic performance. This comparison was conducted by always comparing the dark versus light conditions of the same catalyst, instead comparing the architectures between them. Clear differences in photocatalytic performance were observed depending on the geometry of the structures. We carried out electromagnetic simulations to gain physical insight into how light is absorbed in the bimetallic structure, mapping the location of electromagnetic hotspots leading to the generation of hot carriers. Based on the simulated spectra of light absorption, we performed wavelength and power dependent experiments that unraveled the role of both hot electrons and hot holes when assisting the FA dehydrogenation. These insights can be used to guide the design of improved light harvesting materials for photocatalysis.

2. Results

2.1. Characterization of Bimetallic Nanocatalysts

Figure 1 includes an illustration of the four bimetallic catalysts considered as well as the characterization of representative nanoparticles. The Au NS, which serve as the optical antenna in every catalyst, were synthesized via a seed-mediated approach (Experimental Section), yielding spherical particles whose average diameter was estimated to be 61 ± 1 nm by transmission electron microscopy (TEM) (Figure S1, Supporting Information). The Au antennas were further used for the synthesis of hybrid structures, with either a homogeneous shell or small satellite particles added onto the core particle. A detailed description of the employed syntheses are given in Experimental Section.

Concerning the Au@Pd core–shell structure, we successfully deposited a very thin Pd shell (Figure 1e) on top of the Au NS used as templates. The thickness was estimated to be 1 nm by comparing both Au NS and Au@Pd mean sizes from their respective size distributions (Figure S2, Supporting Information). The material composition of core–shell particles was studied by energy-dispersive X-ray spectroscopy (EDS). As expected, the obtained map confirmed the presence of Pd only at the surface of the nanocatalyst (Figure 1i). Individual maps are provided in Figure S3a, Supporting Information.

As for the Au@AuPd core-bimetallic shell, the TEM (Figure 1f) confirmed an increase in the diameter up to 64 nm due to the reduction of both Au and Pd precursors onto the Au core particle. EDS elemental mapping (Figure 1j, Figure S3b, Supporting Information) confirmed the presence of both metals at the surface. The average composition of the shell at the surface was determined by electrochemical characterization. The shift of the AuPd alloy shell reduction curve to a lower potential than the monometallic counterpart is typical for AuPd alloy with a composition of around 1:1 (Figure S2e, Supporting Information).[40,41] The ICP-AES analysis confirmed an Au-to-Pd ratio of 1:1 for the shell (Table S2, Supporting Information). This alloy has been shown to be the most reactive surface among the possible alloy compositions.[42,43]

As an alternative configuration to the continuous shells of Au@Pd and Au@AuPd, we also considered core-satellites (or antenna-reactor) structures, in which there is a physical gap in between the core and the satellites. This alters completely the decay pathways for captured light, and results in very different

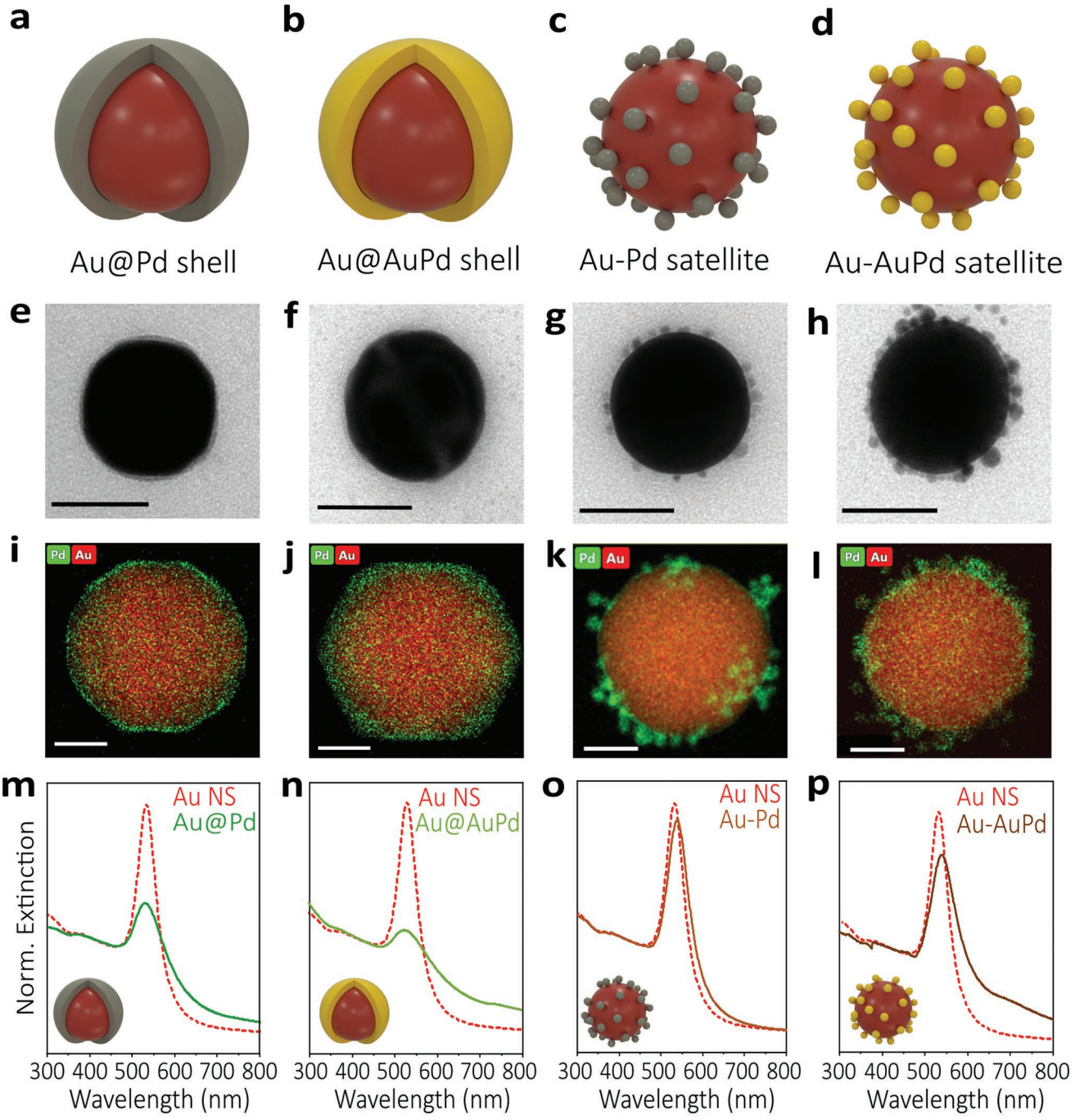

Figure 1. Schematic view of the four catalyst structures. Chemical and optical characterization. a–d) 3D representation of the catalysts used in the photocatalytic experiments. e–h) Bright-field TEM images of representative nanoparticles. The sizes were estimated to be 61 ± 1, 63 ± ~2, and 64 ± ~2 nm for Au NS, Au@Pd, and Au@AuPd, respectively. Pd and AuPd satellites are ≈5 nm in diameter. Scale bars in BF TEM images: 50 nm. i–l) EDS elemental maps of representative nanoparticles. Green and red represent Pd and Au, respectively. Scale bar in EDS images: 20 nm. m–p) Acquired UV–vis spectra for all the catalysts. The bare AuNS spectra are represented by the red dashed line. Extinction spectra are normalized at 400 nm.

photocatalytic activity, as we demonstrate below. For the two antenna-reactor configurations, a full satellite (or reactor) characterization was first performed. The monometallic Pd satellite mean diameter was determined to be 5 nm ± 1 nm, whereas the AuPd satellite was estimated to be 6 ± 1 nm. The colloidal synthesis of the bimetallic satellites yielded small Au nanoparticles coated with a thin Pd shell, confirmed by EDS analysis (Figure S4d, Supporting Information). Additional characterization of the satellites is provided in Figure S4, Supporting Information.

Electron microscopy confirmed the successful attachment of small Pd NPs to Au NS (Figure 1g, Figure S6a, Supporting Information), achieved by solvent-induced electrostatic

self-assembly. This structure was named as Au-Pd core-satellite. The assembly relies on the electrostatic attraction, but also requires EtOH to partially destabilize the cetyl trimethyl ammonium bromide (CTAB) bilayer at the Au surface.[44,45] The remaining CTAB molecules strongly interact with the oppositely charged satellites, driving the assembly. As expected, EDS analysis reveals the presence of Pd satellites (green spots, Figure 1k). From scanning transmission electron microscopy in high-angle annular dark field (STEM-HAADF) images and EDS maps, the satellite density was estimated to be ≈50 Pd satellites per Au NS (Figure S5, Supporting Information).

Following the same methodology, AuPd satellites were also successfully assembled onto the surface of Au NS. Analogously, we named it Au-AuPd core-satellite. TEM images show darker satellites due to the larger contrast of Au (Figure 1h). Correspondingly, elemental mapping confirmed the presence of Au in both the core and the satellites, the latter coated by the thin Pd shell (Figure 1l, Figure S6b, Supporting Information). The homogeneity throughout the core-satellites samples is shown by scanning electron microscopy (SEM) images provided in Figure S5, Supporting Information.

The four catalysts were also characterized optically with UV–vis extinction spectroscopy (Figure 1m–p). Both core–shell structures (Au@Pd and Au@AuPd) showed a typical broader and blue-shifted peak compared to bare Au NS (red dashed line) due to the presence of Pd in the shell, which is more lossy material than Au.[32,46] The alloyed shell also showed a damped plasmon, as a very low amount of the catalytic metal strongly affects the decay pathway.[32] Concerning the Au–Pd core-satellite nanostructure, the plasmon resonance was red-shifted and broadened compared to signal of AuNS, as previously reported for this type of systems.[47] The red shift happens due to changes in the dielectric function in the near-environment of the plasmonic antenna. Finally, the same behavior was observed for the Au-AuPd core-satellite catalyst, although with a larger broadening than Au–Pd, which could be attributed to a broader size distribution. The well-defined resonances of the hybrid structures evidenced the stability of the colloids in solution. A key requirement for our comparisons of photocatalytic activity is that the plasmon resonance fall within the same spectral range, 520–540 nm. This ensures that each catalyst shows a strong interaction with photons of the same energy range. Their optical behavior will be further discussed in the following sections. Once fully characterized, all these structures were tested in photocatalysis experiments.

2.2. Plasmon-Driven Formic Acid Decomposition

To investigate which bimetallic configuration is the most efficient in converting light into chemical energy, we tested the bimetallic catalysts in FA decomposition. For the analysis, we will focus on the improved performance upon illumination, as opposed to the absolute catalytic performance of each configuration.

$$HCOOH \leftrightarrow CO_2 + H_2 (\Delta G = -48.4\ kJ\ mol^{-1}) \quad (1)$$

$$HCOOH \leftrightarrow H_2O + CO (\Delta G = -28.5\ kJ\ mol^{-1}) \quad (2)$$

It is well known that FA decomposition can follow two possible reaction pathways: dehydrogenation, yielding H_2 and carbon dioxide (CO_2) or dehydration forming carbon monoxide (CO) and water (H_2O).[48,49] The former is most favored thermodynamically (Equations (1) and (2)). Note that a little amount of CO can poison the catalyst due to its strong adsorption on Pd surfaces, inactivating the whole catalyst.[50]

Herein, we performed the experiments in a closed reactor with a fine control of the temperature (T = 40.0 ± 0.5 °C) and equal FA concentration (0.5 M) in the absence of any additives (see Experimental Section and Section S6.2, Supporting Information, for experimental details). We aimed to work with both a similar number of Au NS and a similar interface (i.e., capping agents of the colloidal catalysts). The number of Au NS employed in each experiment was estimated by means of their absorption at 400 nm, which corresponds to Au interband transition regime and is relatively unaffected by the plasmon resonance (Section S1, Supporting Information). Concerning the interface, as satellites are coated with polyvinylpyrrolidone (PVP), the capping of core–shell structures (CTAB) was replaced by post-synthesis by dispersing them in a PVP ethanolic solution (Section S4.1, Supporting Information).[51] It allowed us to control the interaction between the Pd surface and FA. The successful exchange was confirmed by ζ-potential measurements (Figure S8, Supporting Information).

It has been recently reported that hot spots formation, which can occur upon aggregation of the particles, has a remarkable influence in plasmonic photocatalysis.[52] Therefore, all the catalysts were supported on 600 nm SiO_2 spheres to avoid the uncontrolled formation of clusters (Figure S9, Supporting Information).

To test the performance of these catalysts in a regime approaching practical applications, we used as light source a commercial solar simulator operated in AM1.5G mode as source of light (P = 125 mW across the visible range). To ensure reproducibility, the catalysis experiments were repeated at least four times each (each of 1 h duration). All these experimental conditions were taken into account to properly address the differences in light-into-chemical conversion efficiency.

As most of the FA decomposition products are gases, a gas chromatograph (GC) equipped with a thermal conductivity detector (TCD) was employed to quantify the reaction rates. Argon (Ar) was used as a carrier gas. To estimate the amount of H_2 produced, a calibration curve was initially obtained by means of standard samples (Figure S10, Supporting Information). The reaction rate was normalized by the amount of Pd present in each sample. Details of these calculations are provided in Section S6.2, Supporting Information.

Control experiments conducted employing Au NS as catalyst in both dark and light conditions showed a significantly lower H_2 generation rate, revealing the Au NS poor catalytic activity in FA decomposition (Figure S11, Supporting Information). Similar controls were also carried out for the particles employed as satellites. The monometallic Pd satellites produced 27 and 22 mmol g Pd^{-1} h^{-1}, whereas the bimetallic AuPd satellites produced 58 and 78 mmol g Pd^{-1} h^{-1} for dark and light tests, respectively. It is worth mentioning that CO was not detected throughout all the performed experiments. These results support the bimetallic synergy for energy conversion, where Au

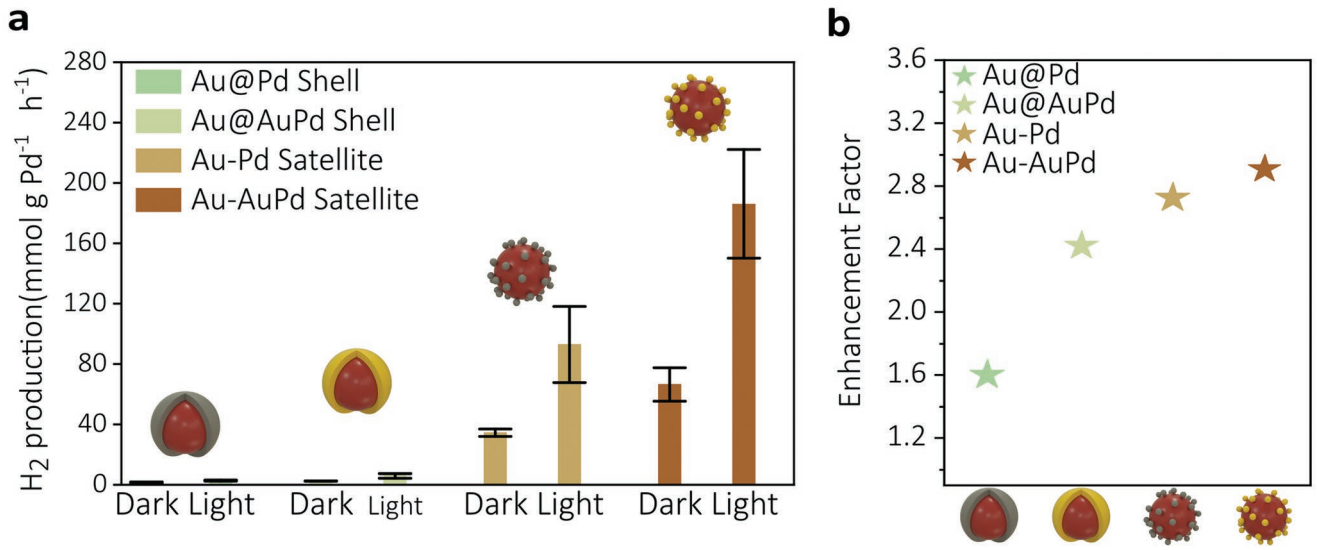

Figure 2. Catalytic performances of bimetallic nanocatalysts in FA decomposition. a) Comparison of H_2 production in dark conditions and upon illumination with solar-simulator (power = 125 mW). The number of Au NS antennas were estimated to be similar in all the experiments and the experiments were repeated at least four times. The FA concentration was 0.5 M in all cases. b) Enhancement factors calculated in all cases as the ratio between light and dark performances.

plays the light confining role and Pd acts as the active catalytic element. All control experiments are presented in Figure S11, Supporting Information.

The H_2 production rates in both dark and light conditions for each bimetallic nanocrystal are shown in **Figure 2**a. The influence of light on the catalytic activity is summarized in the enhancement factor, that is the ratio between illuminated and dark performances (Figure 2b). Core–shell systems showed considerably lower reaction rates in dark and upon illumination compared to the core-satellites structures. Nonetheless, the AuPd alloy shell showed a larger production than the monometallic Pd shell, as expected from the literature on the reactivity of Pd versus the AuPd alloy for this reaction.[42] Likewise, Au@AuPd core–shell also showed a larger enhancement of the light/dark performance (2.4-fold) in comparison with the Au@Pd (1.6-fold) (Figure 2b).

Core-satellites presented a larger production in both dark and light conditions than the core–shell catalysts. The influence of light was slightly higher for these structures, yielding larger enhancement factors when comparing the dark and illuminated cases, and raising the reaction rates 2.7-fold and 2.9-fold for Au–Pd and Au-AuPd systems, respectively. Among all the catalysts, both the largest production and enhancement were displayed by Au-AuPd core-satellites (191 mmol g Pd^{-1} h^{-1}). These results suggest that the two-body architectures are, in principle, the configuration that leads to a larger efficiency for light driven photocatalysis when employing bimetallic plasmonic systems.

2.3. Enhancement Mechanism

FA dehydrogenation is a redox reaction where charge transfers are involved.[53] Briefly, formate ($HCOO^-$, FA^-) adsorbs on Pd in a bridging mode, gets oxidized to CO_2 after C—H bond cleavage and releases one H atom, which is later combined with a second H to yield H_2.[48] As in any chemical reaction, the temperature at the surface of the catalyst plays a major role in the reaction rate due to exponential temperature-dependence of the reaction rate, given by the Arrhenius equation. Besides an increase in temperature, the enhanced absorption of light enabled by the resonant plasmonic antenna can also benefit the catalytic reaction through the generation of hot carriers.[54,55] There has been considerable debate in the recent literature trying to disentangle the two contributions, of heat and of hot carriers, and we therefore took additional steps to try and evaluate heating contributions.

The photocatalysis tests were conducted with a precise control of the temperature, as mentioned above. Likewise, the hybrid catalysts were supported on SiO_2, which enabled us to work with well-separated catalysts avoiding heat accumulation.[56] The stirring conditions employed in the experiments (400 rpm) were high enough to decrease any temperature gradient.[57]

The heat contribution was evaluated as follows. First, we estimated how much the temperature increases due to the illumination for bare Au NS. Barella et al., found a linear dependence of the surface temperature with the irradiance.[58] For a 60 nm Au NS in water and an irradiance of 106 mW cm^{-2}, the temperature is expected to increase only by 5.3×10^{-5} °C (detailed calculation in Section S7, Supporting Information). In a second step, we estimated how much the temperature should be raised to mimic the enhancement for each configuration considering the activation barrier of FA dehydrogenation on Pd, Au, and AuPd (46.6, 53, and 28 kJ mol^{-1}, respectively). These calculations are summarized in Table S4, Supporting Information. While for Pd-FA interfaces, the temperature should increase 10, 21, and 22 K if the enhancement factors are 1.6, 2.7, and 2.9 for Au@Pd core–shell and Au–Pd and Au–AuPd core-satellites, respectively, for Au–FA and AuPd alloy-FA interfaces

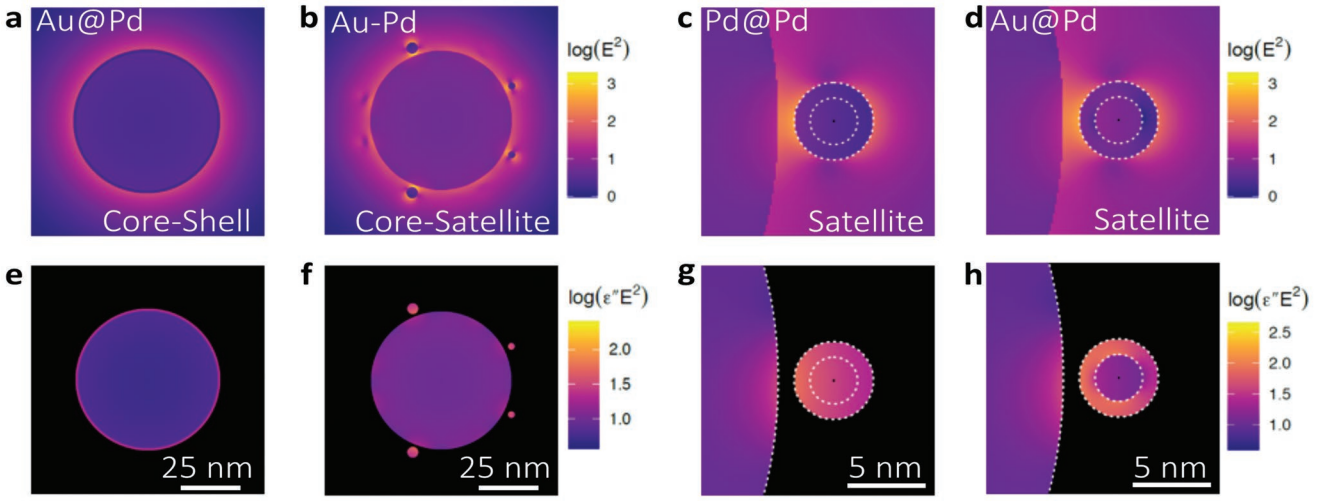

Figure 3. Electric field intensity and absorption maps for bimetallic catalysts. Local field intensity enhancement factor ($|\mathbf{E}|^2$, with unit incident field) for Au@Pd in both a) core–shell and b) core-satellites configuration. Electric field intensity maps for c) a Pd satellite and d) AuPd satellite placed 1 nm away from a 60 nm Au core. Complementary absorption maps of Au@Pd e) core–shell and f) core-satellites. Absorption maps for a full g) Pd satellite and h) AuPd satellite placed at 1 nm away from a 60 nm Au core. In each case the electric field intensity is averaged over incident directions and polarizations.

the temperature should be increased by 34 and 32 K to mimic the enhancement factors (5.6 and 2.4). These crude estimations suggest that the heating coming from the excitation of individual optical antennas (Au NS) is negligible and cannot explain the observed speed up in the reaction rate when the structures are illuminated. Based on all the analysis detailed above, we think the local heat generated upon illumination is not sufficient to explain the observed enhancement and consequently we focused our analysis on the generation of hot carriers.

The absorption of light in a metal such as Pd can lead to a rapid dissipation in the form of direct d-to-s transitions. The presence of a supporting Au antenna can substantially enhance this process through the amplification of the electric field in the Pd region.[52,59,60] The wavelength-dependent ratio of the imaginary part of the dielectric functions of Pd and Au indicates how much light is absorbed dielectric functions of Pd and Au indicates how much light is absorbed per volume unit by the catalytic metal compared to the plasmonic metal under LSPR excitation (Figure S12, Supporting Information). Crucially, we noted differences observed in the extinction spectra of the hybrid catalysts (Figure 1m–p), implying that the absorption in the catalytic active metal can be dependent on the spatial arrangement of the materials. Additionally, the strong inhomogeneous near-field around the satellite particle is expected to boost the generation of hot carriers at the catalyst surface, where they speed up the reaction rate.

To evaluate these differences, we investigated both the electric field intensity and the absorption profiles for each hybrid nanostructure. The geometrical models used in the optical simulations were built up based on the experimental information obtained in their characterization (Figure S7, Supporting Information). **Figure 3** summarizes our efforts to understand how bimetallic catalysts interact with the incoming light and how this may lead to the generation of highly energetic carriers (detailed description of these calculations is provided in Experimental Section). For comparison, the spatial distribution of the near-field at their plasmon resonance is shown for both Au@Pd core–shell (Figure 3a) and Au–Pd core-satellite configurations (Figure 3b). As the satellites consist of either Pd or Au and Pd, Figure 3c,d shows the electric field intensity of a single satellite placed 1 nm away of the 60 nm Au NS antenna. As expected, the electric field at the interparticle gap of an Au–Pd core-satellite structure is ≈30 times larger than the electric field at the surface of Au@Pd core–shell. This is attributed to the small interparticle gap between the two metallic entities, which leads to a hotspot. A non-appreciable difference was observed for mono- and bimetallic satellites, suggesting that the electric field enhancement at the hotspot is not strongly modified by composition of the satellites for that particular size (≈5 nm).

In order to better understand the hot carriers generation within Pd, we also mapped the local rate of absorption, which is proportional to the local field intensity times the imaginary part of the dielectric function in each material region.[52,61] These maps reveal that light is better confined within the Pd satellites than in the 1 nm shell of the core–shell structure, leading to at least a five times larger local absorption rate (Figure 3e,f). For satellites with different composition there is a striking difference. Interestingly, the strongly localized local absorption in the thin Pd shell of the AuPd satellite is higher than in the monometallic Pd satellite (Figure 3g,h). This greater absorption is attributed to the fact that the catalytic metal is placed in between two coupled Au optical antennas. In line with what has already been reported, placing a nonplasmonic metal at the hotspot between two optical antennas, leads to highly confined enhanced absorptions.[52] Indeed, this intense electric field region can account for up to 50% of the hot carriers generation rate,[62] what is beneficial for redox processes as a high carrier density is concentrated in such small spatial region.

Our simulations suggest that core-satellites are more efficient than core–shell structures in funneling the energy from the plasmonic to the catalytic metal. The highly confined and inhomogeneous electric field in the interparticle gap between

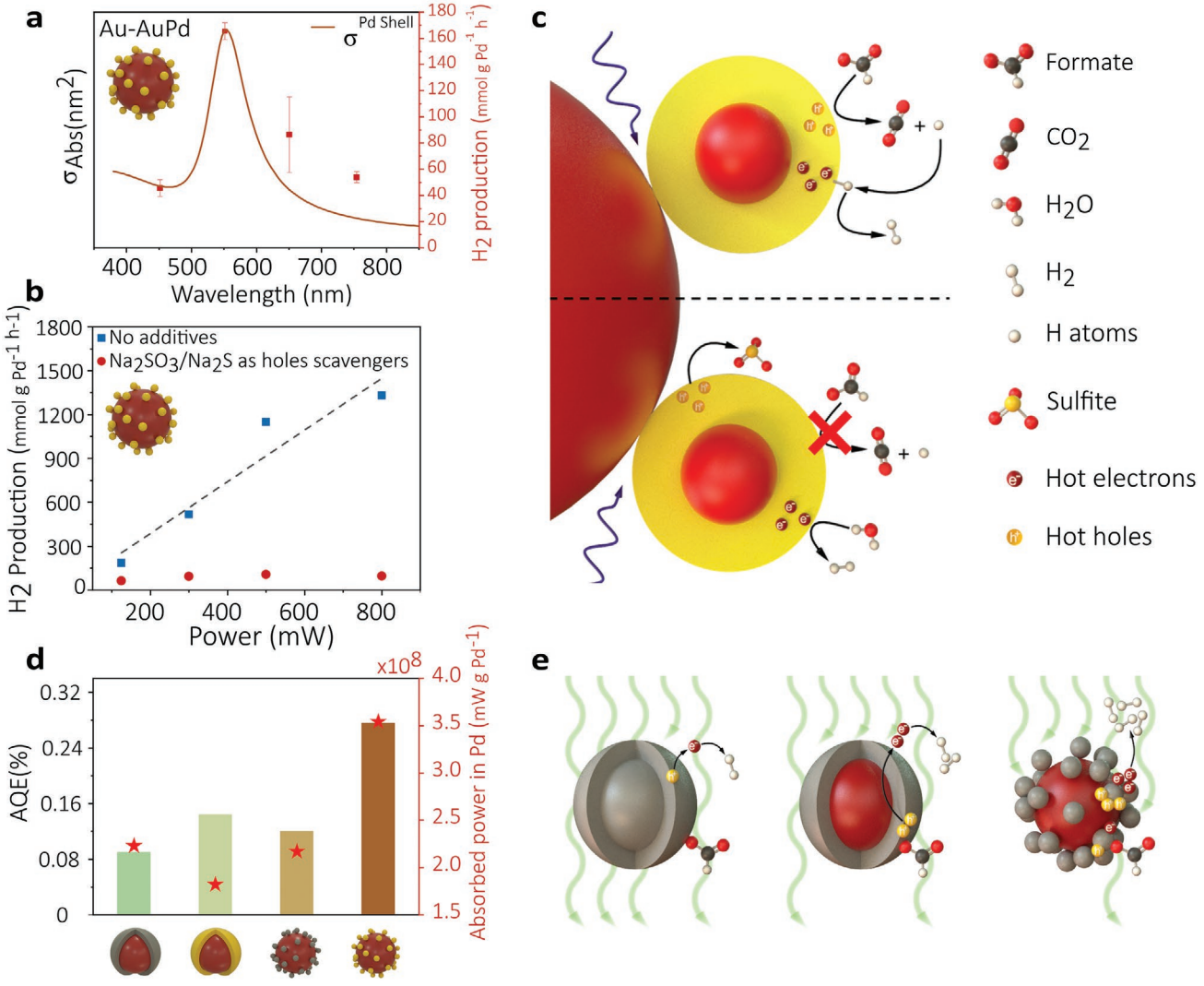

Figure 4. Study of the reaction mechanism. a) Wavelength dependent H_2 production simultaneously plotted with Pd absorption cross-section of Au-AuPd core-satellite nanocatalyst ($N = 4$ for point). b) Power dependent experiments for Au–AuPd core-satellites in the presence and absence of hole scavengers in the reaction mixture ($N = 1$). c) Proposed mechanism of the reaction in the presence and absence of holes scavenger. d) Comparison between the apparent quantum efficiency (AQE) and energy stored on Pd for each structure. The captured power was estimated from electromagnetic simulations, while AQE was estimated at the maximum of the extinction spectra. e) Scheme of Pd partial absorption for different geometries. The presence of hotspots in core-satellite structures leads to a greater Pd absorption.

the core and the satellites, leads to a larger local absorption rate at the surface and therefore a larger local hot carriers generation rate within Pd. Thus, we hypothesize that at the resonance, the hot electrons and the hot holes created in Pd are energetic enough, and present at the surface where the chemical reaction takes place, assisting both the reduction of adsorbed H atoms and the C—H cleavage bond of the FA^-, which is thought to be the rate limiting step of the oxidation reaction.[53]

To test this hypothesis, we conducted wavelength and power dependent FA decomposition experiments on Au–AuPd core-satellite, which turned out to be the more sensitive to light exposure (larger enhancement factor).

For the wavelength dependence, a broadband lamp equipped with bandpass filters of 20 nm width centered at 450, 550, 650, and 750 nm were used. The lamp was additionally equipped with an IR liquid filter to eliminate alternative sources of heat such as water absorption, and with a 400 nm longpass filter to eliminate the UV contribution. The measured power for the aforementioned ranges was 20 mW. We present in Figure 4a the wavelength dependent H_2 production rate. Additionally, as a proxy for the concentration of hot carriers, which remains challenging to calculate in such non-trivial geometries, we also plot in Figure 4a the theoretical spectrum of light absorption in the Pd region of the AuPd satellite. We note a good correlation in the two spectral profiles, especially with the sharp drop of the H_2 production rate obtained when illuminating with blue light (450 ± 10 nm). The long-wavelength tail shows poorer agreement, but this could be explained by the sample inhomogeneity (particle size and gaps); the model considers a single perfectly spherical pair of antenna-satellite, and the

sample's UV–vis characterization already shows a long-wavelength tail (Figure 1). Based on the optical simulations, without the highly confined electric fields, energetic carriers would not be generated within the Pd shell and the reaction could not be sped up, as also shown when the sample is illuminated off-resonance.[63,64] The obtained production using the lamp is comparable to what has been obtained using a solar simulator, as described next.

Another critical measurement to assess the contribution of the absorbed light on the reaction rate is to vary the illumination power (**Figure 4**b). For this, we used a broadband source equipped with the same IR and UV filters. The experiments were conducted without and with hole scavengers ([$NaSO_3$] = 1 mM, [Na_2S] = 1 mM).[65,66] The nature of the additives enables to solely quantify the H_2 generated out of FA. While no additives were added, a linear trend was observed with the increasing power, reaching up to 1331 H_2 mmols g Pd^{-1} h^{-1} when illuminating at 800 mW. However, a remarkable decrease in the activity of the catalyst was observed at all powers in the presence of hole scavengers. This experiment confirms the crucial role of both electrons and holes in the reaction, ruling out the heat contribution. If FA dehydrogenation would have been activated by thermal energy, the reaction rate should have increased with the increasing power when the experiment is performed in the presence of both $NaSO_3$ and Na_2S.

This combination of results leads us to propose that the Pd partial absorption is enhanced when placed in a hotspot between two Au coupled antennas, yielding electrons and holes with sufficient energy to assist the FA dehydrogenation (Figure 4c, upper part). In the presence of a hole scavenger, the holes are partially consumed and, consequently, FA^- is not oxidized to CO_2 (Figure 4c, bottom part). As a result, a second H atom is not released and H_2 production is reduced.[67,68] To restore neutrality in the catalyst, we hypothesize that the excited electron can either reduce the adsorbed H atoms coming from FA acidic dissociation or H_2O molecules.[69].

An important parameter in photocatalysis is the apparent quantum efficiency (AQE), what accounts for how many photoexcited electrons were converted into molecules per incident photon.[9,17,34] The estimated values for our catalysts are shown in Figure 4d (detailed calculations in Section S8, Supporting Information), as well as the energy absorbed by Pd in all the structures. To estimate this captured power (absorption) over the visible range, we integrated the product of the solar simulator spectrum and the Pd partial absorption from 400–800 nm (Section S9, Supporting Information). This total absorbed energy was then normalized by Pd mass. Both the AQE and Pd partial absorption show a dependence on the configuration of the nanoparticle. While the values estimated for Au@Pd, Au@AuPd, and Au–Pd were similar (ranging between 0.08–0.15%), the AQE of Au–AuPd core-satellite was estimated to be 0.28%. This improved AQE was a result of the maximized absorption on the catalytic active metal, as the Au–AuPd structure showed the largest absorption in Pd among all the configurations. These results reinforces the relevance of the geometry on photocatalytic processes. Specifically, the creation of optical hotspots can be converted into chemical hotspots when the active material is placed in such regions of intense and inhomogeneous electric field intensity, maximizing the solar-to-chemical energy conversion capabilities of bimetallic hybrid nanocatalysts. Although these reported values are a lower bound, as we are neglecting optical losses such as scattering, our results demonstrate at least a 3.5 times improvement in AQE when comparing with past reports for similar systems.[70]

We summarize the interpretation of our interpretation of the results in the scheme presented in Figure 4e. A pure Pd NP of ≈5 nm has a very small optical cross-section within the visible range and its catalytic activity relies on its inherent electronic properties. However, when a thin Pd layer (≈1–2 nm) is deposited on an optical antenna, the absorption at the shell is enhanced due to the higher intensity of the electric field. As a result, high energy carriers are created in the active metal, thus speeding up chemical reactions. This phenomenon can be further enhanced by engineering the metals in a two-body structure such as core-satellites. The interaction between two metallic nanoparticles leads to the creation of highly confined electric field regions (optical hotspots) and, consequently, a larger local absorption within the Pd. This results in a larger number of excited carriers and therefore better photocatalytic performances.

Finally, we propose further hybrid nanostructures that can be promising for photocatalysis applications. In such structures a thin shell of either Pd or Au_1Pd_1 (1 nm in thickness) is placed between a 60 nm Au NS and 50 Au satellites of 5 nm in radius. Details of the structures and the calculations is provided in Section S10, Supporting Information. Through optical simulations, we observed that the absorption cross-section does not get significantly boosted with the presence of Au satellites (Figure S14, Supporting Information). Nevertheless, the presence of smaller antennas determines the formation of numerous hotpots, what we have shown that is crucial for hot carriers generation. The optical phenomena dictating the behavior of such hybrid catalysts can be transferred to earth abundant metals such as Cu or Al, preserving the benefits of both the hotspots formation and the catalytic active centers and thus, lowering the overall price of photocatalyst.

3. Conclusions

We demonstrate how plasmonic and catalytic materials should be combined to maximize the conversion of light into chemical energy with hybrid bimetallic plasmonic nanostructures. Core-satellite structures presented larger enhancements on the reaction rate compared to core–shell ones under illumination. The ability to create hotspots strongly influences the energy flow. Our optical simulations indicate at least a fivefold higher local absorption within Pd—the catalytic active metal—when shaped into satellites instead of a thin shell. This enhanced local absorption was manifested as a 30% improvement in the apparent quantum efficiency. Engineering the photocatalyst in a way that the catalytic active metal is placed in the hotspot formed by two optical antennas, as in Au-AuPd, further improves its perfomance. Indeed, this system presented both the largest enhancement factor and apparent quantum efficiency (0.28%).

Energizing the catalytic component of these hybrid materials by increasing local absorption can promote the generation of excited carriers in these typically weakly absorbing materials. Remarkable, the enhanced absorption can be achieved at solar

conditions with the help of the plasmonic counterpart. We envision that plasmonic architectures that maximize the confinement of the nanoscale electric field in the catalytic material will further benefit sunlight into chemical energy conversion processes. Based on our results, colloids with internal hot spots, as well as large-scale metasurfaces and hybrid oligomers, among others, could become key players in the development of the field. Thus, these hybrid plasmonic materials fill the gap of a fundamental prerequisite in the efficient transduction of energy from sunlight to chemistry, which is dealing with solar spectra and irradiances. Toward more sustainable photocatalysis, we strongly believe that the enhanced local absorption on catalytic metals can be driven by earth abundant metals, such as Al or Cu. Similarly, these materials present resonances within the visible range and can achieve a comparable electric field confinement.[71,72]

4. Experimental Section

Chemicals: Gold (III) chloride trihydrate ($HAuCl_4{\cdot}3H_2O$, ≥99.9%), sodium tetrachloropalladate (II) (Na_2PdCl_4, ≥99.9%), potassium tetrachloropalladate (II), (K_2PdCl_4, ≥99.9%), ascorbic acid (AA, ≥99.0%), sodium borohydride ($NaBH_4$, ≥98%), cetyltrimethylammonium bromide (CTAB, ≥99.0%), cetyltrimethyl chloride (CTAC, 25 wt% in water), tetraethylorthosilicate 98% (TEOS), ammonium hydroxide solution (NH_4OH, 28–30% in water), poly(allylamine hydrochloride) (PAH, M_W:17 500), sodium chloride (NaCl, 99%), polyvinylpyrrolidone (PVP, M_W:10 000), formic acid (FA), and absolute ethanol (EtOH) were all purchased from Sigma-Aldrich and used without further purification. In all experiments, ultrapure water with a resistivity of 18.2 MΩ cm was used.

Synthesis of 60 nm Au NS: The Au nanospheres (Au NS) synthesis was performed modifying the seed-mediated growth method described by Zheng et al.[73] These modifications were introduced in order to enlarge the production and favor the reproducibility of photocatalysis experiments.

Au Clusters Preparation: The initial Au clusters were formed by reducing 10 mL of an aqueous solution containing $HAuCl_4$ (0.25 mM) and CTAB (0.1 M) with 600 µL of a freshly prepared 10 mM $NaBH_4$ solution. The solution turns brownish within seconds indicating clusters formation. The clusters were kept undisturbed for 3 h at 27 °C.

10 nm Au NS Synthesis: In a 20 mL glass vial, 4 mL of a 200 mM CTAC solution, and 3 mL of a 100 mM ascorbic acid (AA) solution were mixed, followed by the addition of 100 µL of previously prepared CTAB capped Au clusters. After the solution was stirred at 300 rpm and left at 27 °C for 10 min, 4 mL of 0.5 mM $HAuCl_4$ were added in a quick one-shot injection. The resulting 10 nm Au spheres were centrifuged twice at 13 400 rpm for 30 min and finally redispersed in 1 mL of a 20 mM CTAC solution. These nanoparticles were used as seeds for further growing steps.

60 nm Au NS Synthesis: In order to reach the desired size, 200 mL of a 100 mM CTAC solution were mixed with 1.3 mL of a 100 mM AA solution and 250 µL of 10 nm Au NS solution. The whole solution was kept stirred at 800 rpm at 27 °C for 20 min. Then, 10 mL of 10 mM $HAuCl_4$ were pumped in at a rate of 20 mL h^{-1} and once the pumping completed, was left stirring for 30 min. Even though this rate is ten times larger than the reference, it still yielded 61 nm ± 1.5 nm smooth sphere-like NPs (Figure S1, Supporting Information). After undergoing two centrifugation-redispersion cycles (4000 rpm, 10 min) the Au NS were finally redispersed in 35 mL of mQ H_2O and used for the synthesis of bimetallic nanoparticles.

Synthesis of Au@Pd and Au@AuPd Core–Shell NPs: The core–shell NPs were synthesized by a quick reduction of Pd and Au precursors on top of the previously prepared Au NS. First, as the precursors have different reduction potentials, a ligand exchange was carried out.[74] The precursors solutions (Table S1, Supporting Information) were kept at 100 °C for 60 min. Second, 1.753 mL of an aqueous solution containing ≈ 7.5×10^{11} Au NS were added at 100 °C, followed by the quick injection of 1 mL of 100 mM AA solution. The solutions immediately turned purple and were left at 100 °C for another 60 min. Subsequently, two centrifugation-redispersion cycles (3000 rpm for 10 min) were carried out.

Synthesis of Pd Satellites: PVP-stabilized Pd nanoparticles (Pd NPs) were synthesized according to a method described in the literature with slight modifications.[75] Briefly, an aqueous solution (45 mL) containing PVP (1.05 mM) and AA (4.25 mM) was heated up to 100 °C under reflux for 10 min. Subsequently, an aqueous solution (5.0 mL) containing Na_2PdCl_4 (10 mM) was added. The reaction was allowed to continue at 100 °C for 3 h to obtain Pd NPs.

Synthesis of Au–Pd Satellites: PVP-stabilized Au–Pd nanoparticles (AuPd NPs) were synthesized in an aqueous solution (40 mL) containing PVP (1.05 mM) and AA (4.25 mM) was placed in a three-neck flask fitted with a condenser and refluxed at 100 °C for 10 min. Subsequently, a mixture containing 5.0 mL Na_2PdCl_4 (10 mM) and 5.0 mL $HAuCl_4$ (10 mM) were added in a quick one-shot injection. The reaction was allowed to continue at 100 °C for 3 h to obtain a dark brown solution.

Synthesis of Au–Pd and Au–AuPd core-satellites: 1.4 mL of absolute ethanol were added to 2.77 mL of a 2.72 × ~10^{14} Au NS/L aqueous solution, followed by the addition of 350 µL of non-washed PVP-AA capped satellites (Experimental Section). The solution turned purple within seconds indicating the self-assembly occurrence. After stirring the solution at 400 rpm for 30 min, it was washed in low-binding DNA eppendorf tubes four times at 4000, 3500, and 3000 rpm for 20 min, respectively.

Catalysts Characterization: STEM-HAADF and EDS analysis were performed at 300 kV on a probe corrected Titan Themis equipped with a Super-X EDX detector. TEM characterization was performed on a JEOL JEM-1011 operated at 80 kV. For electron microscopy characterization, the NPs of interest were drop casted from water-based solutions onto carbon/formvar 200 mesh Cu grids. Morphology and the assembly of nanoparticles were observed by using a Zeiss Ultra Plus high-resolution scanning electron microscope (HR-SEM) operated at 10 kV. The extinction spectra of the nanocatalysts were acquired with a Perkin–Elmer UV/Vis/NIR spectrophotometer LAMBDA 750. Zeta potential measurements (ζ) were performed using a Malvern Zetasizer PRO. The electronic properties of the nanoparticles were investigated electrochemically, obtaining the cyclic voltamperogram with a 760 E potentiostat from CH instruments.

Photocatalytic Experiments: The energy conversion experiments were performed in a clean 15 mL reactor containing a flat quartz window (diameter = 1.22 cm) and a rubber septum for sampling. The reactor was placed in a water jacket where water was pumped in and out, allowing to perform the experiments with a precise control of the temperature (40 °C) by means of an external cryostat. During the experiments, the reaction mixture was stirred at 400 rpm using a magnetic bar. The catalysis time was about 1 h and previously bubbled H_2O was used (N_2 for 30 min) in all the experiments. For light experiments, a commercial solar simulator (Newport, VeraSol-2 LED Class AAA) operated in AM1.5G mode was used. The measured incident power was 125 mW within the visible range. For wavelength and power dependent experiments an Arc lamp (Newport, model 66921), where UV contribution was filtered out using a cut-off filter ($\lambda < 400$ nm) and IR contribution was filtered with a IR liquid filter (6123NS). The power was determined using a commercial thermal detector (model: S401C) from Thorlabs. For gas detection, a gas cromatograph from Perkin–Elmer was utilized (Clarus 590 GC), equipped with both a flame ionization detector (FID), to detect organic traces, and a TCD for H_2 detection. In addition, the FID detector was coupled to a H_2 generator from Perkin Elmer (NM plus H2 100).

Electromagnetic Simulations: Numerical simulations were performed with the TERMS program[76,77]—in-house implementation of the superposition T-matrix method by the authors.[78–81] In this approach, the incident and scattered electromagnetic fields were expanded in a basis of vector spherical wavefunctions. The T-matrix of a given particle described the linear relationship between incident and scattered field coefficients. Where multiple scatterers were present, the partial waves

scattered by one particle contributed to the excitation of its neighbors, resulting in a coupled system of equations to be solved for the self-consistent scattered field coefficients. From these, any optical quantity of interest, from far-field cross-sections to near-field quantities could be computed.

A particular strength of this approach was that the T-matrix of a particle, or system of particles, were independent of the incident field. In combination with the basis of spherical waves used to describe incident fields, led to efficient analytical formulas for orientation-averaged quantities, in the far-field[82–84] but also in the near-field.[85,86] Specifically, the scatterer-centred multiple-scattering algorithm of Stout and co-workers,[81] which retained the local-field information. The T-matrix of each particle was calculated from Mie theory, extended to multilayered spheres.[87] To compute the proportion of absorption in each region, the formulas derived by Mackowski were used.[88] The authors were not aware of analytical orientation-averaged formulas having been derived for spherical shells, and used standard numerical averaging instead (six incidence directions).

The system under consideration was challenging, even with state-of-the-art algorithms. Plasmonic metals interacted strongly with light; the plasmon resonances were associated with highly-localized electromagnetic fields. With a numerical method such as finite elements requiring spatial discretization, this would require a very fine mesh to capture the field variations in the satellites, and their outer shell. The T-matrix method was able to describe very fine spatial variations, without any discretization, although the computation cost also increased as higher multipolar orders (N_{Max}) were needed.

For the core–shell antennas, the problem reduced to standard Mie theory and the converged spectra were obtained with few multipoles ($N_{\mathrm{Max}} = 15$). For the antenna-satellites configuration, the computation was much more challenging. Initial simulations were performed with 50 satellites and $N_{\mathrm{Max}} = 25$, but while the spectrum of the whole particle cluster converged to good accuracy (10^{-8} relative error), the absorption in the satellites, of greater relevance here, required even higher multipolar orders. The computations with 50 satellites become difficult on a standard PC, but since the satellite coverage was relatively sparse we can neglect satellite-satellite interactions and simulate the response of a single satellite, with sufficiently high multipolar orders ($N_{\mathrm{Max}} = 35$) for converged results.

Liquid Chromatographic Analysis: The acetaldehyde separation was performed using HPLC-PDA with 150 × 4.6 mm Nova-PAK WATERS C18 column. The mixtures of water/acetonitrile were used as a linear gradient elution profile. The flow rate was set to 1 mL min^{-1} and the injection volume was 20 µL. The PDA detector was 367 nm to record peaks, and standard patron was Carbonyl-DNPH MIX1 from Sigma-Aldrich.

ICP-AES Analysis: Inductively coupled plasma with atomic emission spectroscopy (ICP-AES) was employed to determine both Au and Pd quantities for all samples used in photocatalytic experiments.

The sample preparation was done as follows: right after the test, the SiO_2-supported nanoparticles were collected by centrifugation at 5000 rpm for 15 min and washed by resuspending them in 10 mL of H_2O and centrifuging at same conditions. Finally, the sample was concentrated in 1 mL.

Later on, 500 µL of the concentrated sample were mixed with 500 µL of reversed aqua regia (HNO_3:HCl 3:1) to dissolve metal traces. As for the analysis, 0.5 mL of the last solution were diluted with reversed aqua regia until reaching a final volume of 3.5 mL.

Statistical Analysis: The extinction spectra of the hybrid nanoparticles as well as the Au NS within the visible light were normalized at 400 nm. The generated H_2 moles were determined by determining the peak area in the corresponding gas chromatograph. The Pd load in each experiment was determined by ICP-AES. To obtain the activity of the catalysts, the generated H_2 were normalized by the Pd mass. The individual experiments were averaged ($N = 4$) and the results were reported as mean value ± standard deviation. The size distribution of the catalysts was estimated by ImageJ and the histograms performed in Origin.

Supporting Information

Supporting Information is available from the Wiley Online Library or from the author.

Acknowledgements

The liquid chromatography studies were performed using the facilities in the Seguridade Alimentaria Vigo, Centro de Apoio Científico-Tecnolóxico á Investigación (C.A.C.T.I). The authors thank Miguel Spuch Calvar for his support with the schemes. M.H. and E.C. thank Prof. Sebastian Schlücker, Dr. Roland Grzeschik, and Dr. Elzbieta Stepula for their support. The authors also thank Ms. Edenhofer, Mr. Rath, and Mr. Jahanmehr for their technical and administrative support. M.H. and E.C. thank Prof. Dr. Joachim Rädler and Prof. Dr. Tim Liedl for enabling access to their TEM facilities. B.A. acknowledges support from the Royal Society Te Apārangi through a Rutherford Discovery Fellowship (RDF-VUW1603). The authors acknowledge funding and support from the Deutsche Forschungsgemeinschaft (DFG, German Research Foundation) under Germanys Excellence Strategy –EXC 2089/1 –390776260, the Bavarian program Solar Energies Go Hybrid (SolTech), the Center for NanoScience (CeNS) and the European Commission through the ERC Starting Grant CATALIGHT (802989). A.S.C. acknowledges Xunta de Galicia, Spain, for her postdoctoral fellowship. C.F. acknowledges Nankai University, China, for his visiting research fellowship.

Open access funding enabled and organized by Projekt DEAL.

Conflict of Interest

The authors declare no conflict of interest.

Data Availability Statement

The data that support the findings of this study are available from the corresponding author upon reasonable request.

Keywords

hybrid bimetallic plasmonics, hydrogen production, plasmon-driven photocatalysis

Received: March 25, 2022
Revised: June 16, 2022
Published online: July 7, 2022

[1] S. Chen, T. Takata, K. Domen, *Nat. Rev. Mater.* **2017**, *2*, 17050.
[2] C. Wang, D. Astruc, *Chem. Soc. Rev.* **2021**, *50*, 3437.
[3] K. Daehn, R. Basuhi, J. Gregory, M. Berlinger, V. Somjit, E. A. Olivetti, *Nat. Rev. Mater.* **2021**, *7*, 275.
[4] J. Eppinger, K.-W. Huang, *ACS Energy Lett.* **2017**, *2*, 188.
[5] J.-M. Lavoie, *Front. Chem.* **2014**, *2*, 81.
[6] L. Zhou, J. M. P. Martirez, J. Finzel, C. Zhang, D. F. Swearer, S. Tian, H. Robatjazi, M. Lou, L. Dong, L. Henderson, P. Christopher, E. A. Carter, P. Nordlander, N. J. Halas, *Nat. Energy* **2020**, *5*, 61.
[7] H. Song, X. Meng, T. D. Dao, W. Zhou, H. Liu, L. Shi, H. Zhang, T. Nagao, T. Kako, J. Ye, *ACS Appl. Mater. Interfaces* **2018**, *10*, 408.
[8] S. Luo, H. Lin, Q. Wang, X. Ren, D. Hernández-Pinilla, T. Nagao, Y. Xie, G. Yang, S. Li, H. Song, M. Oshikiri, J. Ye, *J. Am. Chem. Soc.* **2021**, *143*, 12145.

[9] S. Ezendam, M. Herran, L. Nan, C. Gruber, Y. Kang, F. Gröbmeyer, R. Lin, J. Gargiulo, A. Sousa-Castillo, E. Cortés, *ACS Energy Lett.* **2022**, *7*, 778.
[10] P. Camargo, E. Cortés, *Plasmonic Catalysis: From Fundamentals to Applications*, Wiley, New York **2021**.
[11] S. Linic, P. Christopher, D. B. Ingram, *Nat. Mater.* **2011**, *10*, 911.
[12] E. Cortés, W. Xie, J. Cambiasso, A. S. Jermyn, R. Sundararaman, P. Narang, S. Schlücker, S. A. Maier, *Nat. Commun.* **2017**, *8*, 14880.
[13] P. Christopher, H. Xin, S. Linic, *Nat. Chem.* **2011**, *3*, 467.
[14] S. Li, H. Huang, L. Shao, J. Wang, *ACS Nano* **2021**, *15*, 10759.
[15] E. Cortés, *Science* **2018**, *362*, 28.
[16] U. Aslam, S. Chavez, S. Linic, *Nat. Nanotechnology* **2017**, *12*, 1000.
[17] B. Seemala, A. J. Therrien, M. Lou, K. Li, J. P. Finzel, J. Qi, P. Nordlander, P. Christopher, *ACS Energy Lett.* **2019**, *4*, 1803.
[18] S. Mukherjee, F. Libisch, N. Large, O. Neumann, L. V. Brown, J. Cheng, J. B. Lassiter, E. A. Carter, P. Nordlander, N. J. Halas, *Nano Lett.* **2013**, *13*, 240.
[19] J. Gargiulo, R. Berté, Y. Li, S. A. Maier, E. Cortés, *Acc. Chem. Res.* **2019**, *52*, 2525.
[20] E. Oksenberg, I. Shlesinger, A. Xomalis, A. Baldi, J. J. Baumberg, A. F. Koenderink, E. C. Garnett, *Nat. Nanotechnol.* **2021**, *16*, 1378.
[21] G. Tagliabue, J. S. DuChene, M. Abdellah, A. Habib, D. J. Gosztola, Y. Hattori, W.-H. Cheng, K. Zheng, S. E. Canton, R. Sundararaman, J. Sá, H. A. Atwater, *Nat. Mater.* **2020**, *19*, 1312.
[22] J. Quiroz, E. C. Barbosa, T. P. Araujo, J. L. Fiorio, Y.-C. Wang, Y.-C. Zou, T. Mou, T. V. Alves, D. C. de Oliveira, B. Wang, S. J. Haigh, L. M. Rossi, P. H. C. Camargo, *Nano Lett.* **2018**, *18*, 7289.
[23] M. Vadai, D. K. Angell, F. Hayee, K. Sytwu, J. A. Dionne, *Nat. Commun.* **2018**, *9*, 4658.
[24] J. A. Esterhuizen, B. R. Goldsmith, S. Linic, *Chem* **2020**, *6*, 3100.
[25] S. Li, P. Miao, Y. Zhang, J. Wu, B. Zhang, Y. Du, X. Han, J. Sun, P. Xu, *Adv. Mater.* **2021**, *33*, 2000086.
[26] K. Sytwu, M. Vadai, F. Hayee, D. K. Angell, A. Dai, J. Dixon, J. A. Dionne, *Science* **2021**, *371*, 280.
[27] H. Robatjazi, J. L. Bao, M. Zhang, L. Zhou, P. Christopher, E. A. Carter, P. Nordlander, N. J. Halas, *Nat. Catal.* **2020**, *3*, 564.
[28] Z. Li, D. Kurouski, *Acc. Chem. Res.* **2021**, *54*, 2477.
[29] K. Sytwu, M. Vadai, J. A. Dionne, *Adv. Phys.: X* **2019**, *4*, 1619480.
[30] D. Liu, C. Xue, *Adv. Mater.* **2021**, *33*, 2005738.
[31] S. Wang, J. Yao, Z. Ou, X. Wang, Y. Long, J. Zhang, Z. Fang, T. Wang, T. Ding, H. Xu, *Nanoscale* **2022**, *14*, 4705.
[32] C. Engelbrekt, K. T. Crampton, D. A. Fishman, M. Law, V. A. Apkarian, *ACS Nano* **2020**, *14*, 5061.
[33] S. Linic, S. Chavez, R. Elias, *Nat. Mater.* **2021**, *20*, 916.
[34] K. Li, N. J. Hogan, M. J. Kale, N. J. Halas, P. Nordlander, P. Christopher, *Nano Lett.* **2017**, *17*, 3710.
[35] C. Zhang, H. Zhao, L. Zhou, A. E. Schlather, L. Dong, M. J. McClain, D. F. Swearer, P. Nordlander, N. J. Halas, *Nano Lett.* **2016**, *16*, 6677.
[36] D. F. Swearer, R. K. Leary, R. Newell, S. Yazdi, H. Robatjazi, Y. Zhang, D. Renard, P. Nordlander, P. A. Midgley, N. J. Halas, E. Ringe, *ACS Nano* **2017**, *11*, 10281.
[37] C. Zhan, Q.-X. Wang, J. Yi, L. Chen, D.-Y. Wu, Y. Wang, Z.-X. Xie, M. Moskovits, Z.-Q. Tian, *Sci. Adv.* **2021**, *7*, 10eabf0962.
[38] J. U. Salmón-Gamboa, M. Romero-Gómez, D. J. Roth, A. V. Krasavin, P. Wang, W. Dickson, A. V. Zayats, *Nanoscale Adv.* **2021**, *3*, 767.
[39] E. Cortés, L. V. Besteiro, A. Alabastri, A. Baldi, G. Tagliabue, A. Demetriadou, P. Narang, *ACS Nano* **2020**, *14*, 16202.
[40] M. Valenti, N. P. Prasad, R. Kas, D. Bohra, M. Ma, V. Balasubramanian, L. Chu, S. Gimenez, J. Bisquert, B. Dam, W. A. Smith, *ACS Catal.* **2019**, *9*, 3527.
[41] V. Pifferi, C. E. Chan-Thaw, S. Campisi, A. Testolin, A. Villa, L. Falciola, L. Prati, *Molecules* **2016**, *21*, 261.
[42] S.-J. Li, Y.-T. Zhou, X. Kang, D.-X. Liu, L. Gu, Q.-H. Zhang, J.-M. Yan, Q. Jiang, *Adv. Mater.* **2019**, *31*, 1806781.
[43] C.-R. Kao, Y.-C. Huang, B. Talukdar, Y.-C. Chuang, Y.-R. Lu, H.-M. Lin, W.-C. Chou, D. A. Cullen, C.-L. Dong, C.-H. Kuo, *ACS Appl. Energy Mater.* **2021**, *4*, 2652.
[44] M. Grzelczak, L. M. Liz-Marzán, R. Klajn, *Chem. Soc. Rev.* **2019**, *48*, 1342.
[45] H. Hu, F. Ji, Y. Xu, J. Yu, Q. Liu, L. Chen, Q. Chen, P. Wen, Y. Lifshitz, Y. Wang, Q. Zhang, S.-T. Lee, *ACS Nano* **2016**, *10*, 7323.
[46] Z.-Q. Tian, B. Ren, J.-F. Li, Z.-L. Yang, *Chem. Commun.* **2007**, *34*, 3514.
[47] Y. Li, Y. Hu, F. Shi, H. Li, W. Xie, J. Chen, *Angew. Chem., Int. Ed.* **2019**, *58*, 9049.
[48] K. Tedsree, T. Li, S. Jones, C. W. A. Chan, K. M. K. Yu, P. A. Bagot, E. A. Marquis, G. D. Smith, S. C. E. Tsang, *Nat. Nanotechnol.* **2011**, *6*, 302.
[49] W.-Y. Yu, G. M. Mullen, D. W. Flaherty, C. B. Mullins, *J. Am. Chem. Soc.* **2014**, *136*, 11070.
[50] H.-X. Zhang, S.-H. Wang, K. Jiang, T. André, W.-B. Cai, *J. Power Sources* **2012**, *199*, 165.
[51] M. Mao, B. Zhou, X. Tang, C. Chen, M. Ge, P. Li, X. Huang, L. Yang, J. Liu, *Chem. Eur. J.* **2018**, *24*, 4094.
[52] S. Lee, H. Hwang, W. Lee, D. Schebarchov, Y. Wy, J. Grand, B. Auguié, D. H. Wi, E. Cortés, S. W. Han, *ACS Energy Lett.* **2020**, *5*, 3881.
[53] B. Wu, J. Lee, S. Mubeen, Y.-S. Jun, G. D. Stucky, M. Moskovits, *Adv. Opt. Mater.* **2016**, *4*, 1041.
[54] Y. Dubi, I. W. Un, Y. Sivan, *Chem. Sci.* **2020**, *11*, 5017.
[55] P. K. Jain, *J. Phys. Chem. C* **2019**, *123*, 24347.
[56] G. Baffou, P. Berto, E. Bermúdez Ureña, R. Quidant, S. Monneret, J. Polleux, H. Rigneault, *ACS Nano* **2013**, *7*, 6478.
[57] I.-W. Un, Y. Sivan, *ACS Photonics* **2021**, *8*, 1183.
[58] M. Barella, I. L. Violi, J. Gargiulo, L. P. Martinez, F. Goschin, V. Guglielmotti, D. Pallarola, S. Schlücker, M. Pilo-Pais, G. P. Acuna, S. A. Maier, E. Cortés, F. D. Stefani, *ACS Nano* **2021**, *15*, 2458.
[59] S. Chavez, U. Aslam, S. Linic, *ACS Energy Lett.* **2018**, *3*, 1590.
[60] D. F. Swearer, H. Zhao, L. Zhou, C. Zhang, H. Robatjazi, J. M. P. Martirez, C. M. Krauter, S. Yazdi, M. J. McClain, E. Ringe, E. A. Carter, P. Nordlander, N. J. Halas, *Proc. Natl. Acad. Sci. USA* **2016**, *113*, 8916.
[61] G. Baffou, R. Quidant, *Laser Photonics Rev.* **2013**, *7*, 171.
[62] L. V. Besteiro, X.-T. Kong, Z. Wang, G. Hartland, A. O. Govorov, *ACS Photonics* **2017**, *4*, 2759.
[63] E. Pensa, J. Gargiulo, A. Lauri, S. Schlücker, E. Cortés, S. A. Maier, *Nano Lett.* **2019**, *19*, 1867.
[64] E. Y. Santiago, L. V. Besteiro, X.-T. Kong, M. A. Correa-Duarte, Z. Wang, A. O. Govorov, *ACS Photonics* **2020**, *7*, 2807.
[65] J.-L. Yang, Y.-L. He, H. Ren, H.-L. Zhong, J.-S. Lin, W.-M. Yang, M.-D. Li, Z.-L. Yang, H. Zhang, Z.-Q. Tian, J.-F. Li, *ACS Catal.* **2021**, *11*, 5047.
[66] P. Rodenas, T. Song, P. Sudhagar, G. Marzari, H. Han, L. Badia-Bou, S. Gimenez, F. Fabregat-Santiago, I. Mora-Sero, J. Bisquert, U. Paik, Y. S. Kang, *Adv. Energy Mater.* **2013**, *3*, 176.
[67] Y. Kim, S.-h. Kim, H. C. Ham, D. H. Kim, *J. Catal.* **2020**, *389*, 506.
[68] M. Navlani-García, K. Mori, D. Salinas-Torres, Y. Kuwahara, H. Yamashita, *Front. Mater.* **2019**, *6*, 44.
[69] Z. Lou, M. Fujitsuka, T. Majima, *ACS Nano* **2016**, *10*, 6299.
[70] Z. Zheng, T. Tachikawa, T. Majima, *J. Am. Chem. Soc.* **2014**, *136*, 6870.
[71] P. R. West, S. Ishii, G. V. Naik, N. K. Emani, V. M. Shalaev, A. Boltasseva, *Laser Photonics Rev.* **2010**, *4*, 795.
[72] G. V. Naik, J. L. Schroeder, X. Ni, A. V. Kildishev, T. D. Sands, A. Boltasseva, *Opt. Mater. Express* **2012**, *2*, 478.
[73] Y. Zheng, X. Zhong, Z. Li, Y. Xia, *Part. Part. Syst. Charact.* **2014**, *31*, 266.

[74] S.-C. Hsu, Y.-C. Chuang, B. T. Sneed, D. A. Cullen, T.-W. Chiu, C.-H. Kuo, *Nano Lett.* **2016**, *16*, 5514.
[75] B. Lim, M. Jiang, J. Tao, P. H. Camargo, Y. Zhu, Y. Xia, *Adv. Funct. Mater.* **2009**, *19*, 189.
[76] D. Schebarchov, A. Fazel-Najafabadi, E. C. Le Ru, B. Auguié, *J. Quant. Spectrosc. Radiat. Transfer* **2022**, *284*, 108131.
[77] D. Schebarchov, E. C. L. Ru, J. Grand, B. Auguié, *Opt. Express* **2019**, *27*, 35750.
[78] D. W. Mackowski, M. I. Mishchenko, *J. Opt. Soc. Am. A* **1996**, *13*, 2266.
[79] M. I. Mishchenko, L. D. Travis, A. A. Lacis, *Scattering, Absorption, and Emission of Light by Small Particles*, Cambridge University Press, Cambridge **2002**.
[80] B. Stout, J.-C. Auger, J. Lafait, *J. Mod. Opt.* **2002**, *49*, 2129.
[81] B. Stout, J. C. Auger, A. Devilez, *J. Opt. Soc. Am. A* **2008**, *25*, 2549.
[82] R. N. S. Suryadharma, C. Rockstuhl, *Materials* **2018**, *11*, 2.
[83] N. G. Khlebtsov, *Appl. Opt.* **1992**, *31*, 5359.
[84] M. Mishchenko, *Sov. Astron. Lett.* **1989**, *15*, 299.
[85] J.-C. Auger, B. Stout, *Appl. Opt.* **2008**, *47*, 2897.
[86] A. Fazel-Najafabadi, S. Schuster, B. Auguié, *Phys. Rev. B* **2021**, *103*, 115405.
[87] E. Le Ru, P. Etchegoin, *Principles of Surface-Enhanced Raman Spectroscopy: And Related Plasmonic effects*, Elsevier, New York **2008**.
[88] D. W. Mackowski, R. A. Altenkirch, M. P. Menguc, *Appl. Opt.* **1990**, *29*, 1551.